ADVANCED ENERGY MATERIALS
www.advenergymat.de

$NiCo_2O_4$ Nanofibers as Carbon-Free Sulfur Immobilizer to Fabricate Sulfur-Based Composite with High Volumetric Capacity for Lithium–Sulfur Battery

*Ya-Tao Liu, Dian-Dian Han, Lu Wang, Guo-Ran Li, Sheng Liu, and Xue-Ping Gao**

Both the energy density and cycle stability are still challenges for lithium–sulfur (Li–S) batteries in future practical applications. Usually, light-weight and nonpolar carbon materials are used as the hosts of sulfur, however they struggle on the cycle stability and undermine the volumetric energy density of Li–S batteries. Here, heavy $NiCo_2O_4$ nanofibers as carbon-free sulfur immobilizers are introduced to fabricate sulfur-based composites. $NiCo_2O_4$ can accelerate the catalytic conversion kinetics of soluble intermediate polysulfides by strong chemical interaction, leading to a good cycle stability of sulfur cathodes. Specifically, the S/$NiCo_2O_4$ composite presents a high gravimetric capacity of 1125 mAh g^{-1} at 0.1 C rate with the composite as active material, and a low fading rate of 0.039% per cycle over 1500 cycles at 1 C rate. In particular, the S/$NiCo_2O_4$ composite with the high tap density of 1.66 g cm^{-3} delivers large volumetric capacity of 1867 mAh cm^{-3}, almost twice that of the conventional S/carbon composites.

1. Introduction

The exploration for high energy storage systems has become more urgent, in order to meet the growing energy demand of portable electronic devices and electric vehicles. Among various alternatives, lithium–sulfur (Li–S) battery is the most potential candidate due to the high theoretical energy density of 2600 Wh kg^{-1} or 2800 Wh L^{-1} on the basis of mass or volume, respectively.[1] The energy density of 500 Wh kg^{-1} is set to be a target for practical Li–S battery in the near future, which is almost 20% of the theoretical energy density based on mass calculation. However, the volumetric energy density of 550–600 Wh L^{-1} (still 20% of the theoretical energy density of Li–S battery) has already been achieved years ago in commercial Li-ion batteries with heavy $LiCoO_2$ as cathode.[2] Therefore, the enhancement of the volumetric capacity of the sulfur cathode should be a primary concern in order to maintain high volumetric energy density of Li–S battery, simultaneously accompanied with high gravimetric energy density.

The cycle stability is another key factor for practical application of Li–S battery.[3] In the dissolution–deposition reaction of sulfur cathode, soluble lithium polysulfides (LiPS) are unavoidable, which are sources of the shuttle effect and low utilization of sulfur, as well as the low cycle stability.[4] The most common strategy in the recent years is to physically confine sulfur in various carbon materials, such as meso/microporous carbons,[5] carbon nanotubes,[6] carbon fibers,[7] graphene (oxide),[8] carbon spheres.[9] However, such non- or weak-polar carbon materials only offer weak interactions toward polar LiPS, making against the long-term cycle stability of sulfur cathode. In order to enhance the affinity and catalytic conversion of intermediate LiPS, the heteroatom modification is introduced into carbon hosts, based on the contribution of nitrogen doping to the interaction with LiPS.[10] More recently, polar compounds, such as metal oxides,[11] sulfides,[12] nitrides,[13] carbides,[14] phosphides,[15] and MXene[16] are also used as sulfur hosts for improving the cycle stability through the polar interaction between hosts and LiPS. In particular, the catalytic conversion kinetics of intermediate LiPS can be accelerated, which are beneficial to reduce the accumulation of sulfides on cathode and to weak the shuttle effect.[17] Nevertheless, these compounds are usually supported on carbon materials,[12a,b,13b,14a,18] unfavorable for the improvement on the volumetric capacity of sulfur-based composites.

Therefore, based on the consideration of the volumetric energy density and cycle stability, heavy and polar transition metal oxides (TMOs) are expected to be potential candidates of sulfur hosts in Li–S battery. On the one hand, as compared with conventional light-weight carbon materials, TMOs are heavy with higher density (≈4.5 g cm^{-3}), making them possible to fabricate sulfur-based composites with high tap density. On the other hand, the polar affinity of TMOs is helpful for facilitating the catalytic conversion of polar intermediate LiPS in charge–discharge processes, leading to good cycle stability of sulfur-based composites.

As typical TMOs, spinel nickel cobaltite ($NiCo_2O_4$) possesses the high density up to 5.6 g cm^{-3},[19] which could be desirable host materials to fabricate sulfur-based composite with high tap

Y.-T. Liu, D.-D. Han, L. Wang, G.-R. Li, S. Liu, Prof. X.-P. Gao
Institute of New Energy Material Chemistry
School of Materials Science and Engineering
Renewable Energy Conversion and Storage Center
Nankai University
Tianjin 300350, China
E-mail: xpgao@nankai.edu.cn

The ORCID identification number(s) for the author(s) of this article can be found under https://doi.org/10.1002/aenm.201803477.

DOI: 10.1002/aenm.201803477

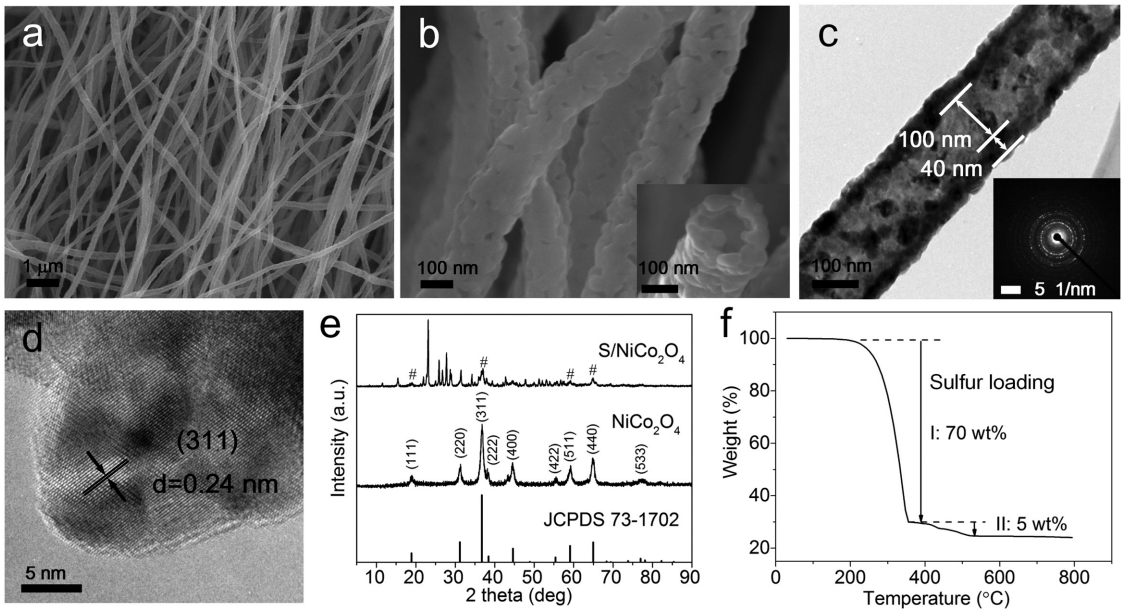

Figure 1. Characterization of the $NiCo_2O_4$ nanofibers and $S/NiCo_2O_4$ composite. a,b) Scanning electron microscope (SEM) images of $NiCo_2O_4$ nanofibers. c) TEM image of $NiCo_2O_4$ nanofibers and the corresponding SAED pattern. d) HRTEM image of $NiCo_2O_4$ nanofibers. e) XRD patterns of $NiCo_2O_4$ nanofibers and $S/NiCo_2O_4$ composite. The diffraction peaks of $NiCo_2O_4$ are marked with pound signs in the pattern of $S/NiCo_2O_4$ composite. f) TG curve of the $S/NiCo_2O_4$ composite in Ar atmosphere.

density. Moreover, $NiCo_2O_4$ is a mixed valence oxide with good electronic conductivity, in which redox couples of Co^{3+}/Co^{2+} and Ni^{3+}/Ni^{2+} coexist.[20] The polar feature of $NiCo_2O_4$ is beneficial to adsorption and subsequent catalytic conversion of polar intermediate LiPS, which is demonstrated in electrocatalysis of water splitting.[21] The feasibility of $NiCo_2O_4$ hollow microtubes as sulfur host was verified previously by Iqbal et al.[22] However, the sulfur content on $NiCo_2O_4$ microtubes was extremely low (27 wt%), far from the requirement for cathode with high sulfur content. In this contribution, 1D $NiCo_2O_4$ nanofibers are prepared and used as carbon-free host of sulfur with high content. The 1D nanostructure could provide good conductive networks and ion diffusion paths in the dissolution–deposition processes of sulfur cathode, and simultaneously provide enough active sites for the catalytic conversion of polar intermediate LiPS, based on the requirement for increasing both the gravimetric capacity and volumetric capacity.

2. Results and Discussion

2.1. Preparation and Characterization of the $S/NiCo_2O_4$ Composite

Figure S1 in the Supporting Information shows a schematic illustration of the preparation of the $S/NiCo_2O_4$ composite. In a typical procedure, pristine nanofibers are first obtained by electrospinning the solution of polyacrylonitrile (PAN), cobalt acetate, and nickel acetate. Then, pristine nanofibers are calcined at 500 °C for 3 h in air to get hollow $NiCo_2O_4$ nanofibers with removing PAN template. Next, hollow $NiCo_2O_4$ nanofibers are dispersed in deionized water by sonication, followed by dropping into sulfur–amine solution.[23] Sulfur is in situ deposited on $NiCo_2O_4$ nanofibers when diluted HNO_3 is dropwise added into the above suspension. Finally, the $S/NiCo_2O_4$ composite is obtained after centrifugation, rinsing, and drying.

The $NiCo_2O_4$ nanofibers are tens of micrometers long with a uniform diameter of ≈150–200 nm (**Figure 1**a,b). The nanofibers, composed of irregular nanocrystals, have a hollow structure and rough surface. The formation of hollow structure is ascribed to the decomposition of PAN template during calcination.[24] As shown in transmission electron microscope (TEM) image (Figure 1c), the inner diameter and outer wall thickness of the $NiCo_2O_4$ nanofibers are about 100 and 40 nm, respectively. The nanofibers have a polycrystalline characteristics, as confirmed by the clear diffraction rings in selected area electron diffraction (SAED) pattern (Figure 1c, inset). In crystallographic structure, $NiCo_2O_4$ is assigned to the cubic spinel structure (JCPDS 73-1702) (Figure 1e). The average crystallite size of $NiCo_2O_4$ is estimated as 13.7 nm by Scherrer equation.[25] In the high resolution transmission electron microscope (HRTEM) image (Figure 1d), the lattice spacing of 0.247 nm can be observed clearly, corresponding to the dominant exposed (311) plane of the cubic structure as indicated in X-ray diffraction (XRD) pattern. The (111) and (220) planes are also visible in HRTEM images (Figure S2, Supporting Information). After loading sulfur, the strong diffraction peaks of $NiCo_2O_4$ are still detected in the $S/NiCo_2O_4$ composite (Figure 1e), accompanied with the appearance of orthorhombic sulfur. The sulfur content is 75 wt% in the $S/NiCo_2O_4$ composite, as shown in thermogravimetric (TG) curve with two steps of weight loss due to the strong chemical binding between $NiCo_2O_4$ and sulfur (Figure 1f). The sulfur distribution is relatively homogeneous among $NiCo_2O_4$ nanofibers, coexisting with nickel, cobalt, and oxygen elements as detected by the elemental mappings (**Figure 2**). In the meantime, the sulfur loading results in the dramatic decline of the specific surface area from 241 to 55 $m^2\ g^{-1}$ (Figure S3, Table S1,

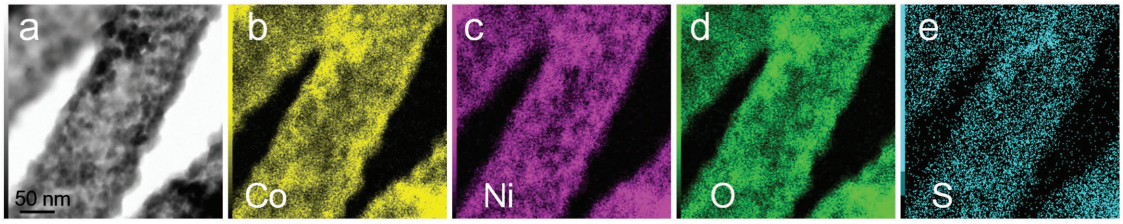

Figure 2. Characterization of the S/$NiCo_2O_4$ composite. a) TEM image of the S/$NiCo_2O_4$ composite. b–e) Elemental mappings of (b) Co, (c) Ni, (d) O, and (e) S in the selected region of the S/$NiCo_2O_4$ composite.

Supporting Information), due to the coverage of sulfur inside hollow structure or on the outer surface of $NiCo_2O_4$ nanofibers. Similarly, hollow carbon nanofibers (CNF) with a diameter of 400 nm are also presented as a contrast sample (Figure S4, Supporting Information) for preparing the S/CNF composite.

2.2. Electrochemical Performance of the S/$NiCo_2O_4$ Composite

The electrochemical performance is evaluated in standard 2032 coin cells. The sulfur content is 52.5 wt% in the whole cathode, including all binder/conducting agents. The capacity is calculated based on the composite as active material unless noted specifically. As shown in **Figure 3**a, the S/$NiCo_2O_4$ composite delivers the high gravimetric capacity of 1125 mAh $g^{-1}_{\text{-composite}}$ at 0.1 C rate, corresponding to 1500 mAh $g^{-1}_{\text{-sulfur}}$ based on sulfur mass (high sulfur utilization of 89.5%), which is 1.2 times that of the S/CNF composite. The dramatically changeable expression on capacity can be identified in the volumetric capacity because of the significant difference on tap density of heavy oxide or light-weight carbon hosts. Here, the tap densities of the S/$NiCo_2O_4$ and S/CNF composites are estimated as 1.66 and 0.96 g cm^{-3}, respectively. The volumetric capacity of the S/$NiCo_2O_4$ composite is calculated to be 1867 mAh $cm^{-3}_{\text{-composite}}$, while the S/CNF composite only exhibits lower volumetric capacity of 850 mAh $cm^{-3}_{\text{-composite}}$ (Figure 3b). The volumetric capacity of the S/$NiCo_2O_4$ composite is almost twice that of the S/CNF composite. It is well known that the theoretical density of sulfur is only 2.07 g cm^{-3}. It means that both the high tap density of 1.66 g cm^{-3} and large volumetric capacity

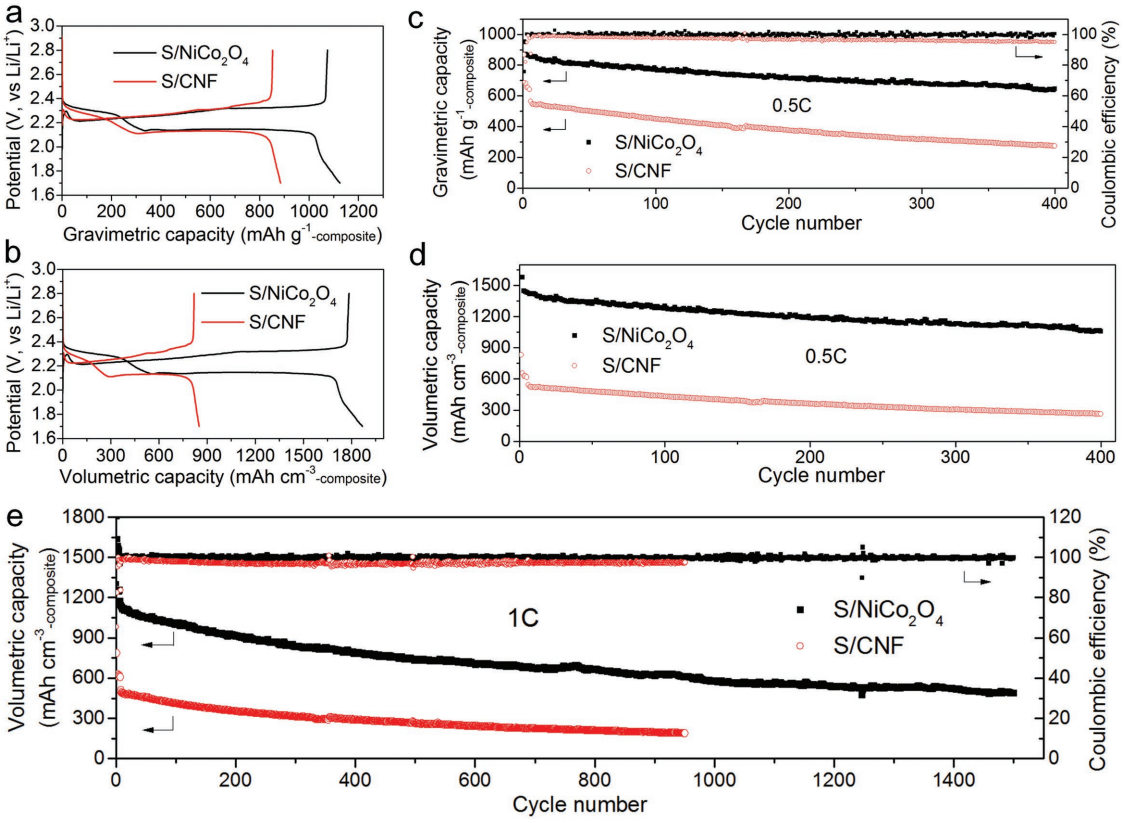

Figure 3. Electrochemical performance of the S/$NiCo_2O_4$ and S/CNF composites (electrolyte/sulfur ratio: 25 µL mg^{-1}, sulfur loading: 1.3–1.5 mg cm^{-2}). a,b) Comparison of discharge–charge profiles of the S/$NiCo_2O_4$ and S/CNF composites at 0.1 C rate. (a) Gravimetric capacity and (b) volumetric capacity. c,d) Cycle performance of the S/$NiCo_2O_4$ and S/CNF composites at 0.5 C rate. (c) Gravimetric capacity and (d) volumetric capacity. e) Long-term cycle performance of the S/$NiCo_2O_4$ and S/CNF composites at 1 C rate.

of 1867 mAh $cm^{-3}_{\text{-composite}}$ are desirable values for the S-based composite. The technology strategy is feasible and favorable for ensuring the high volumetric energy density of practical Li–S battery, which is also demonstrated in sulfur/ferrite composites.[26] In Figure 3c,d, the cycle performance of the S/$NiCo_2O_4$ and S/CNF composites is compared based on gravimetric capacity and volumetric capacity, respectively. At 0.5 C rate, the S/$NiCo_2O_4$ composite displays the gravimetric capacity of 872 mAh $g^{-1}_{\text{-composite}}$, corresponding to the volumetric capacity of 1447 mAh $cm^{-3}_{\text{-composite}}$, superior to that of the S/CNF composite (654 mAh $g^{-1}_{\text{-composite}}$ and 628 mAh $cm^{-3}_{\text{-composite}}$). After 400 cycles, the high reversible capacity of 646 mAh $g^{-1}_{\text{-composite}}$ is still retained with a low fading rate of 0.065% per cycle for the S/$NiCo_2O_4$ composite. The long-term cycle stability is also obtained at high rate (Figure 3e). At 1 C rate, the large initial capacity of 1171 mAh $cm^{-3}_{\text{-composite}}$ can be released for the S/$NiCo_2O_4$ composite. After 1500 cycles, the capacity of 487 mAh $cm^{-3}_{\text{-composite}}$ is maintained with high Coulombic efficiency (>99.5%) and very low fading rate of 0.039% per cycle. In contrast, the discharge capacity and cycle stability at 1 C rate are unsatisfactory for the S/CNF composite.

Under normal conditions, carbon materials as sulfur hosts are superior on electronic conductivity as compared with TMOs, which is important for achieving good high-rate capability of S-based composites. However, the S/$NiCo_2O_4$ composite presents good rate performance (**Figure 4**a). Especially, at 5 C rate, the S/$NiCo_2O_4$ composite still delivers larger discharge capacity of 400 mAh $g^{-1}_{\text{-composite}}$, with both the high and low discharge potential plateaus. While the S/CNF composite can only be discharged at 2 C rate with lower discharge capacity of 143 mAh $g^{-1}_{\text{-composite}}$ (Figure 4b). Actually, only the first high discharge potential plateau appears at 2 C rate for the S/CNF composite due to large polarization. It means that the high rate capability of the S-based composites is dominated by the kinetic factor, rather than electronic conductivity of sulfur hosts. In the meantime, the good redox kinetics on $NiCo_2O_4$ nanofibers are also beneficial to the high sulfur loading, which is necessary in practical application. When the sulfur loadings are set to be 2, 3, and 4 mg cm^{-2}, the S/$NiCo_2O_4$ composite can release high discharge capacities of 868, 873, and 834 mAh g^{-1} at 0.1 C rate, respectively (Figure S5, Supporting Information). Moreover, the good cycle performance is obtained at the sulfur loading of 4 mg cm^{-2} (Figure S6, Supporting Information).

Low electrolyte loading is necessary for fabricating Li–S battery with high energy density,[27] under the condition of ensuring the good electrochemical performance of cathode. Therefore, the performance of S/$NiCo_2O_4$ composite is further evaluated with different electrolyte/sulfur (E/S) ratios (Figure 4c). Indeed, the high E/S ratio (25 µL mg^{-1}) is superior to show the desirable electrochemical performance, especially the low potential polarization and high discharge capacity, due to the effective wetting and penetration of electrolyte across the electrode/electrolyte interface. At the E/S ratio of 10 µL mg^{-1}, the composite still presents high electrochemical capacity and good cycle stability at 0.5 C rate (Figure 4d). Theoretically, the lean electrolyte could increase the electrolyte viscosity and decrease the utilization of sulfur, due to the dissolution of LiPS in electrolyte. When the E/S ratio is decreased to 5 µL mg^{-1}, the discharge capacity of 940 mAh $g^{-1}_{\text{-composite}}$ (1253 mAh $g^{-1}_{\text{-sulfur}}$) is obtained at 0.1 C rate, slightly lower as compared with the high electrolyte loading. Meanwhile, larger potential polarization appears, leading to the slight decrease of two potential

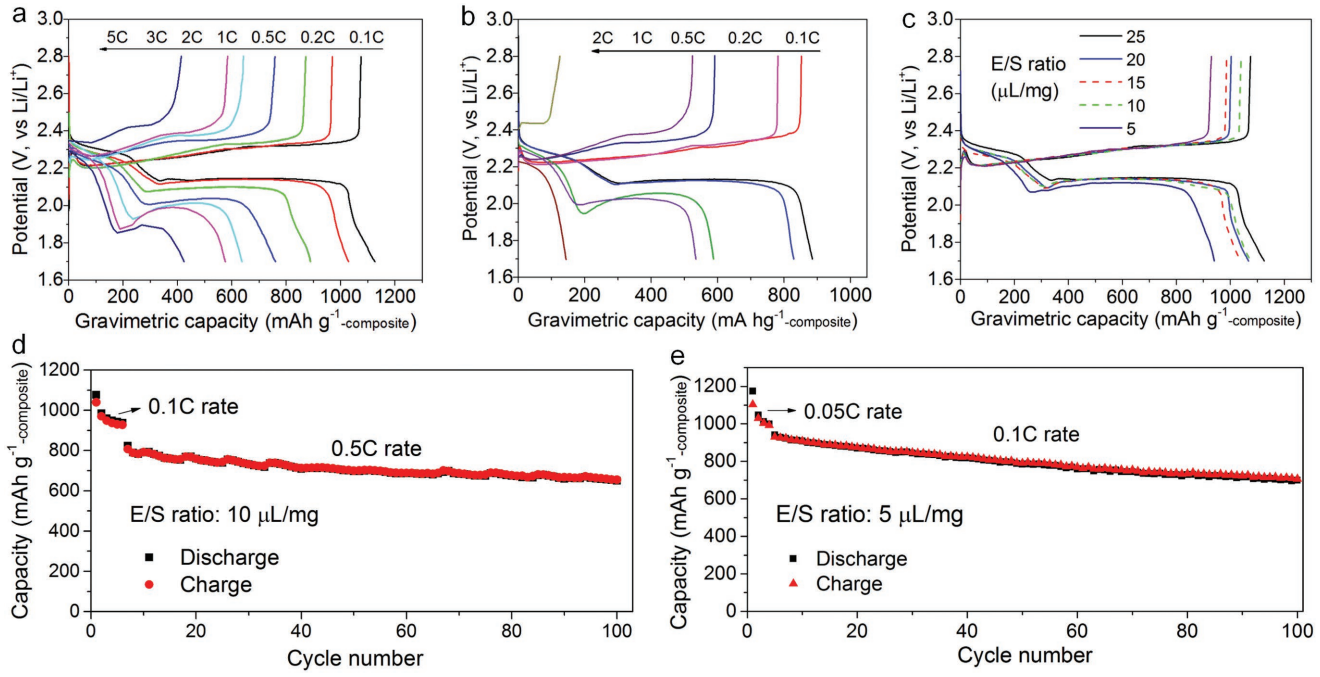

Figure 4. Discharge–charge curves of the a) S/$NiCo_2O_4$ and b) S/CNF composites at various rates. c) Discharge–charge curves of the S/$NiCo_2O_4$ composite (sulfur loading of 1.5 mg cm^{-2}) at 0.1 C rate with different E/S ratios. d) The cycling performance of the S/$NiCo_2O_4$ composite at 0.5 C rate with the E/S ratio of 10 µL mg^{-1} (S loading: 1.5 mg cm^{-2}). e) The cycling performance of the S/$NiCo_2O_4$ composite at 0.1 C rate with the E/S ratio of 5 µL mg^{-1} (S loading: 1.5 mg cm^{-2}).

plateaus in the discharge process. Impressively, the S/$NiCo_2O_4$ composite with a low E/S ratio of 5 µL mg^{-1} displays a good cycling stability within 100 cycles at 0.1 C rate (Figure 4e). As a result, $NiCo_2O_4$ proves to be a promising alternative to carbon hosts in fabricating efficient S-based composite. Nevertheless, it should be noted that $NiCo_2O_4$ does not compete against carbon materials in terms of conductivity. Therefore, conducting agent (carbon nanotubes) is still indispensable in porous sulfur cathode, which can provide a good conducting network for electron transport and a porous supporting framework for electrolyte diffusion.

A series of metal cobaltites MCo_2O_4 (M = Mg, Mn, Cu, and Zn) are also examined to justify the common feature of metal cobaltites as sulfur hosts. Under optimized conditions, all the sulfur/cobaltite composites can deliver large initial capacity over 1000 mAh $g^{-1}_{\text{-composite}}$ at 0.1 C rate (Figure S8, Supporting Information). Specifically, the S/$MnCo_2O_4$ composite exhibits the good cycle performance at 1 C rate among all the composites, with a low fading rate of 0.079% per cycle (Figure S9, Supporting Information). It means that it is a common feature to use metal cobaltites as efficient sulfur hosts, which could be extended to more heavy TMOs for fabricating dense sulfur-based composites with high tap density and high volumetric capacity.

The true densities of *a*-S_8 and Li_2S are 2.07 and 1.66 g cm^{-3}, respectively. In Li–S cell, the volume expansion and shrink of the sulfur cathode occur inevitably during repeated cycling due to the difference of the true density between active material (S) and discharged product (Li_2S). In this work, we focus on the volumetric capacity of the sulfur-based composites, and such sulfur-based composites are key materials to obtain the sulfur cathode. When the sulfur contents in the composites are similar (70 wt%), the volume expansion and shrink are almost identical for the sulfur cathode with different hosts. In future work, the volumetric capacity of the sulfur cathode should be considered further, not only the sulfur-based composites.

2.3. Redox Kinetics of LiPS in the S/$NiCo_2O_4$ Composite

Usually, the typical electrochemical process follows three stages: diffusion, adsorption, and charge-transfer processes on the electrode surface. Here, LiPS as intermediate are soluble in the electrochemical process from insoluble sulfur to insoluble Li_2S, where the diffusion, adsorption, and charge-transfer processes are involved. In particular, the catalytic conversion of soluble intermediate LiPS is a crucial step in the electrochemical dissolution/deposition processes of sulfur cathode. Here, $NiCo_2O_4$ nanofibers act not only as sulfur host, but also as good electrocatalyst to accelerate the redox kinetics of soluble intermediate LiPS in the electrochemical reaction of sulfur cathode. **Figure 5**a shows typical cyclic voltammograms (CVs) of the S/$NiCo_2O_4$ and S/CNF composites. The two sharp cathodic peaks at 2.29 and 2.0 V (vs Li/Li^+) are associated with the stepwise reduction of sulfur to soluble intermediate LiPS and insoluble final Li_2S, respectively. In the anodic scan, two sharp peaks at 2.32 and 2.41 V (vs Li/Li^+) are also observed, which are assigned to the reverse conversion. On the contrary, the redox peaks of S/CNF composite are relatively broadened, simultaneously accompanied with the slight shift of the reduction peaks to the low potential. It means that the better reversibility of the redox reaction can be realized under catalysis of $NiCo_2O_4$ nanofibers in the S/$NiCo_2O_4$ composite.

To further probe the effect of $NiCo_2O_4$ nanofibers on the redox kinetics of soluble intermediate LiPS, CV measurements are conducted under different scan rates (Figure S10, Supporting Information). It is demonstrated that the redox peak currents appear as a linear relationship with the square root of scan rate (Figure 5b–d), implying that the rate determined step is dominated by the diffusion process of LiPS. Thus, the lithium ion diffusion process can be described by the Randles–Sevcik equation[28]:

$$I_p = (2.69\times10^5)n^{1.5}AD^{0.5}Cv^{0.5}(25^\circ\text{C})$$

where I_p is the peak current (A), n is the charge transfer number, A is the active electrode area (cm^2), D is the lithium ion diffusion coefficient (cm^2 s^{-1}), C is the concentration of Li ions (mol cm^{-3}), and v is the scan rate (V s^{-1}). Since n, A, C in the cell can be regarded as constant, the slope of plots ($I_p/v^{0.5}$) reflects the diffusion rate of Li ions, which offers critical information on the kinetics of polysulfides conversion. In particular, the slopes in the reduction/oxidation peaks (*a*, *b*, and *c*) are relatively larger for the S/$NiCo_2O_4$ composite as compared with those of the S/CNF composite (Table S2, Supporting Information), indicating the faster diffusion process of soluble intermediate LiPS due to the introduction of $NiCo_2O_4$ nanofibers. The faster diffusion is mainly related to the strong adsorption of LiPS on $NiCo_2O_4$ surface, which is an essential procedure for the subsequent electrocatalysis.[28] The CV feature in symmetric cells with Li_2S_6 electrolyte could provide further evidence for the electrocatalysis. Compared with CNF electrode, the over-potentials for the redox reaction of sulfur in $NiCo_2O_4$ electrode are relatively low (Figure S11, Supporting Information), indicating a high electrochemical activity of LiPS on $NiCo_2O_4$ electrode.

Next, in situ electrochemical impedance spectra (EIS) are presented here to investigate the electrochemical processes at the electrode/electrolyte interface. At the secondary and low potential plateau of the discharge process, Nyquist plots are consisted of two semicircles and a slope line (Figure 5e), which are associated with the charge-transfer, adsorption, and diffusion processes of soluble intermediate LiPS, respectively. The charge-transfer resistance (R_{ct}), adsorption impedance, and diffusion impedance are smaller for the S/$NiCo_2O_4$ composite, further confirming the improved redox kinetics of soluble intermediate LiPS on $NiCo_2O_4$ nanofibers. Moreover, EIS measurement at different discharge/charge stages offers more details in the conversion kinetics of intermediate LiPS (Figures S12 and S13, Supporting Information). As shown in Figure S12 in the Supporting Information, the selected points for EIS test correspond to the stepwise reduction of sulfur during discharge and the subsequent reverse oxidation during charge. Compared with S/CNF composite, the S/$NiCo_2O_4$ composite shows smaller charge-transfer resistance (R_{ct}), adsorption impedance, and diffusion impedance (Figure S13, Supporting Information; Table S3). It implies that $NiCo_2O_4$ could accelerate both the reduction and oxidation process of intermediate LiPS, acting as bifunctional catalyst.

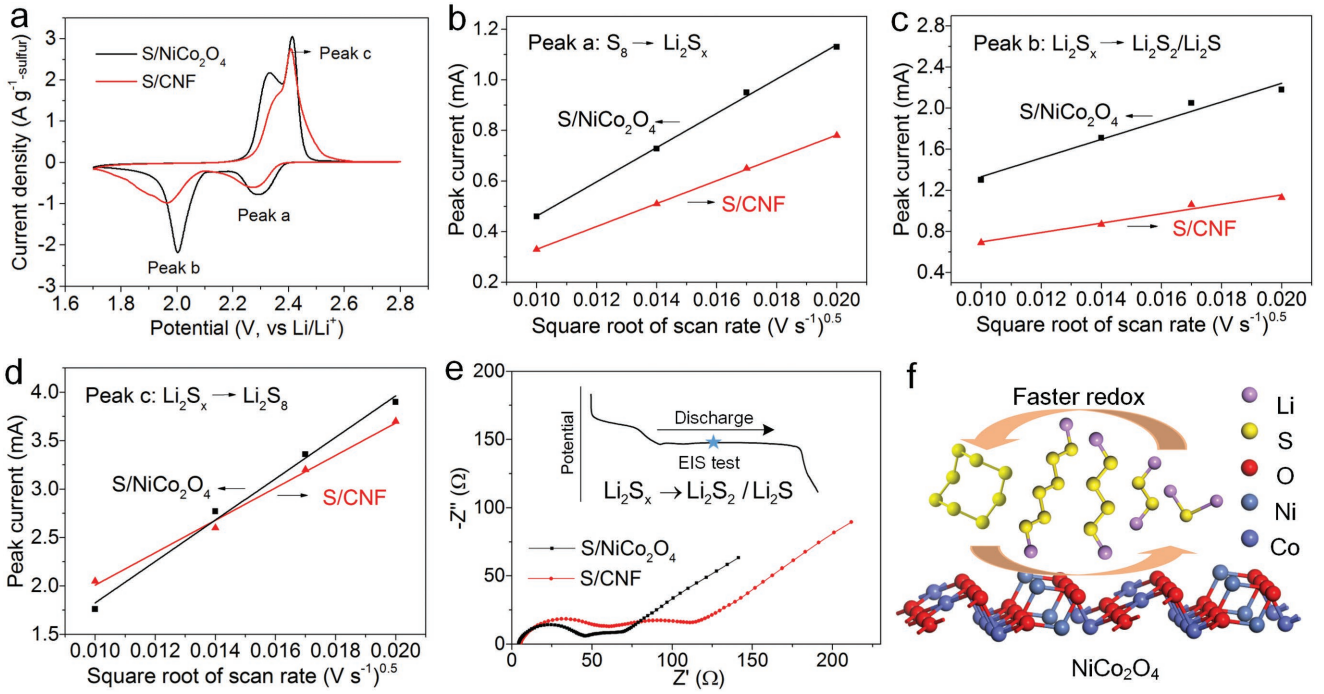

Figure 5. Kinetics of the catalytic conversion of LiPS in the S/$NiCo_2O_4$ and S/CNF composites. a) CVs of the S/$NiCo_2O_4$ and S/CNF composites at the scan rate of 0.1 mV s^{-1}. b–d) The relationships between the peak current and scan rate for different reaction processes in the S/$NiCo_2O_4$ and S/CNF composites. (b) Peak *a*: $S_8 \rightarrow Li_2S_x$, (c) Peak *b*: $Li_2S_x \rightarrow Li_2S_2/Li_2S$, (d) Peak *c*: $Li_2S_x \rightarrow S_8$ ($4 \leq x \leq 8$). e) Nyquist plots of the S/$NiCo_2O_4$ and S/CNF composites at the secondary and low potential plateau of the discharge process. Nyquist plots at different DOD and depth of charge (DOC) are shown in Figures S12 and S13 in the Supporting Information. f) A schematic showing the faster redox kinetics of LiPS on the $NiCo_2O_4$ surface.

The (111), (220), and (311) planes can be observed in HRTEM images (Figure S2, Supporting Information), while the (311) plane is shown as the most intensive peak in XRD patterns. It means that the (311) plane is dominant in all exposed planes of spinel $NiCo_2O_4$, which was also observed in previous publications.[29] In the meantime, as compared to low-indexed planes (111 and 220) with close-packed arrays of atoms, the surface energy is higher for the (311) plane, which is more favorable to adsorb LiPS for stabilizing the surface. In particular, the high electrocatalytic activity and strong adsorption of soluble intermediate LiPS occur on the dominant exposed (311) plane of $NiCo_2O_4$ nanofibers, which was demonstrated previously to be effective in Li-ion batteries and water splitting.[29] Herein, active Ni and Co atoms could provide energetic reaction sites to adsorb polar LiPSs and catalyze conversion kinetics of soluble intermediate LiPS, as illustrated in Figure 5f.

The high electrochemical activity can drive the conversion of soluble intermediate LiPS and increase the utilization of sulfur in the electrochemical dissolution/deposition reaction, resulting in the larger reversible capacity. Based on the evaluation from above CVs and EIS, $NiCo_2O_4$ nanofibers show higher electrochemical activity to promote the conversion of soluble intermediate LiPS as compared with CNF host. The immediate and effective consequence is to reduce the potential polarization, and to increase the utilization of sulfur and gravimetric capacity of the S/$NiCo_2O_4$ composite. After taking into account the high tap density (1.66 g cm^{-3}), the volumetric capacity is more advantageous for the S/$NiCo_2O_4$ composite.

2.4. Entrapment of LiPS on $NiCo_2O_4$ Nanofibers

In the electrochemical dissolution–deposition processes of the sulfur cathode, the intermediate LiPS are soluble, which provides a good chance to in situ observe the adsorption process of LiPS. To demonstrate the adsorption, optically transparent cells are fabricated (inset in **Figure 6**a), where the color is chosen as an indicator of soluble LiPS in electrolyte. Photos are taken at different depths of discharge (DOD). Before discharging, the electrolyte of two cells without any LiPS is colorless and transparent. When the cells are discharged to 200 mAh $g^{-1}$$_{-composite}$ (the first high potential plateau), there are still no obvious color observed in electrolyte with limited LiPS. After discharging to 600 mAh $g^{-1}$$_{-composite}$ (the second low potential plateau), the bright yellow can be observed obviously in the cell with the S/CNF composite as cathode. This potential region corresponds to the slow conversion of soluble Li_2S_4 with a relatively high concentration. At the end of discharge, the yellow color fades slightly due to the formation of insoluble Li_2S_2 and Li_2S. The poor adsorption of soluble LiPS is the reason to produce the yellow color in electrolyte. Clearly, in the cell with the S/$NiCo_2O_4$ composite as cathode, the pale yellow is observed in the low potential region due to the adsorption of soluble LiPS. At the end of discharge, the electrolyte becomes almost colorless and transparent again. The adsorption of soluble LiPS on $NiCo_2O_4$ nanofibers can be further confirmed in the static experimental test and UV–vis spectra (Figure 6b), in which Li_2S_4 is expressed as a representative species of LiPS. The superior capability of $NiCo_2O_4$ nanofibers to adsorb Li_2S_4

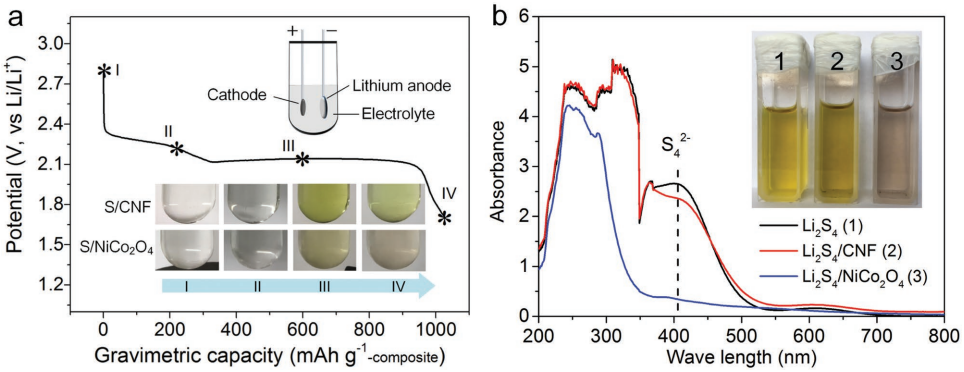

Figure 6. Visual observation of LiPS entrapment on $NiCo_2O_4$ nanofibers and CNFs in dynamic and static processes. a) In situ observation of the transparent electrolyte in Li–S cells at different DOD. I: before discharging (0 h), II: discharged to 200 mAh g^{-1}-composite (3 h), III: discharged to 600 mAh g^{-1}-composite (13 h), IV: end of discharge (20 h). b) Demonstration of the static adsorption of Li_2S_4 on $NiCo_2O_4$ nanofibers and CNFs. UV–vis spectra of supernatant of Li_2S_4 solution after the adsorption test, and the corresponding photos (inset).

can be observed visually from the colorless solution, which is attributed to the strong chemical interaction between $NiCo_2O_4$ and LiPS. In contrast, the weak chemical interaction exists in Li_2S_4/CNF solution with the retentive bright yellow color. Especially in UV–vis spectra, the characteristic absorbance of S_4^{2-} at 410 nm disappears after the static adsorption with $NiCo_2O_4$, indicative of the absence of Li_2S_4 in the solution.[30] It means that the adsorption entrapment of soluble LiPS is strong on $NiCo_2O_4$ nanofibers, which is beneficial to the subsequent catalytic conversion of soluble LiPS, as well as the stable cycle performance of the S/$NiCo_2O_4$ composite.

2.5. Chemical Interaction Between $NiCo_2O_4$ and LiPS

The nature of the interaction between $NiCo_2O_4$ and Li_2S_4 is further investigated by XPS spectra of Co $2p_{3/2}$, Ni $2p_{3/2}$, and S 2p. Herein, $NiCo_2O_4$ presents the strong chemical interaction with LiPS, owing to the Co^{3+}/Co^{2+} and Ni^{3+}/Ni^{2+} couples on the active (311) plane.[29] As shown in **Figure 7**a, before interacting with Li_2S_4 solution, the Co $2p_{3/2}$ core level is consisted of Co^{2+} at 781.1 eV and Co^{3+} at 779.7 eV, with 28.6% fraction of Co^{3+}. After interacting with Li_2S_4 solution, the fraction of Co^{3+} is decreased to 21.9% (Figure 7b). In the Ni $2p_{3/2}$ core level of pure $NiCo_2O_4$, the peaks at 854.3 and 855.9 eV are assigned as Ni^{2+} and Ni^{3+}, respectively (Figure 7c). Similarly, after interacting with Li_2S_4 solution, the fraction of Ni^{3+} is decreased from 86.3% to 81.8% (Figure 7d). It means that both Co^{3+} and Ni^{3+} are partially reduced, attributed to the charge transfer from S_4^{2-} in Li_2S_4 solution. This explanation is evidenced by the appearance of significant peaks at higher binding energy (165–171 eV) of sulfur species (Figure 7e). After interacting with $NiCo_2O_4$, there are two multiple S 2p spectra, which are separated into four sulfur environments. The peak at 163.2 eV is the contribution from the bridging sulfur (S_B^0) of Li_2S_4, and the peak at 161.9 eV is originated from the terminal sulfur (S_T^{-1}) or sulfides.[11a,31] The signals at 166.7 and 168.7 eV are attributed to thiosulfate and polythionate complex, respectively.[32] It is found that polythionate species can be reversibly formed by the oxidation of $NiCo_2O_4$ (Figure S14, Supporting Information), and the similar mechanism was demonstrated previously by the oxidation effect of MnO_2, VO_2, and V_2O_5 on LiPS.[11a,33] These polythionate species, acting as a mediator, could alleviate the shuttle issue. Furthermore, all the peaks of Co^{2+}/Co^{3+} and Ni^{2+}/Ni^{3+} shift to lower binding energy by 0.4–0.7 eV after interacting with Li_2S_4, which is ascribed to the strong chemical affinity between LiPS and Ni/Co cations.[34] Figure 7f illustrates the chemical interaction on $NiCo_2O_4$ nanofibers. It is believed that the chemical interaction is the intrinsic driving force to adsorb and catalyze soluble LiPS on $NiCo_2O_4$ surface. Such chemical interaction could be generally formed when polar hosts of sulfur are introduced, such as TiO,[35] Co_3O_4,[36] ZnS,[37] prussian blue,[38] as well as N-doped carbon materials,[39] which brings sulfur cathode a good cycling performance to a great extent.[40]

As additional evidence for the good entrapment of soluble LiPS, the surface corrosion of Li anode by soluble LiPS during cycling should be weakened, which is highly important for application of Li–S cells.[41] As shown in Figure S15 in the Supporting Information, the smooth surface of Li anode with slight cracks can be observed for the cell with S/$NiCo_2O_4$ cathode after 100 cycles. Additionally, S mapping on the Li anode surface is mild, indicating the effective conversion of soluble LiPS with less Li_2S/Li_2S_2 deposition. For the cell with S/CNF cathode, the Li anode suffers severe surface damage with more cracks. Along with such cracks, the surface corrosion of Li anode by soluble LiPS is more obvious. Therefore, the good entrapment of soluble LiPS on $NiCo_2O_4$ is effective not only for enhancing the cycle stability of sulfur cathode, but also for stabilizing Li anode during cycling.

3. Conclusion

Both the gravimetric and volumetric energy densities are important for Li–S battery, which are mainly dominated by sulfur cathode. Different from the conventional light-weight carbon materials as sulfur host, using heavy TMOs as sulfur host is one of the feasible technological approaches to fabricate dense sulfur-based composites with high tap density. Specifically, in this work, carbon-free porous hollow $NiCo_2O_4$ nanofibers are used to fabricate the S/$NiCo_2O_4$ composite with

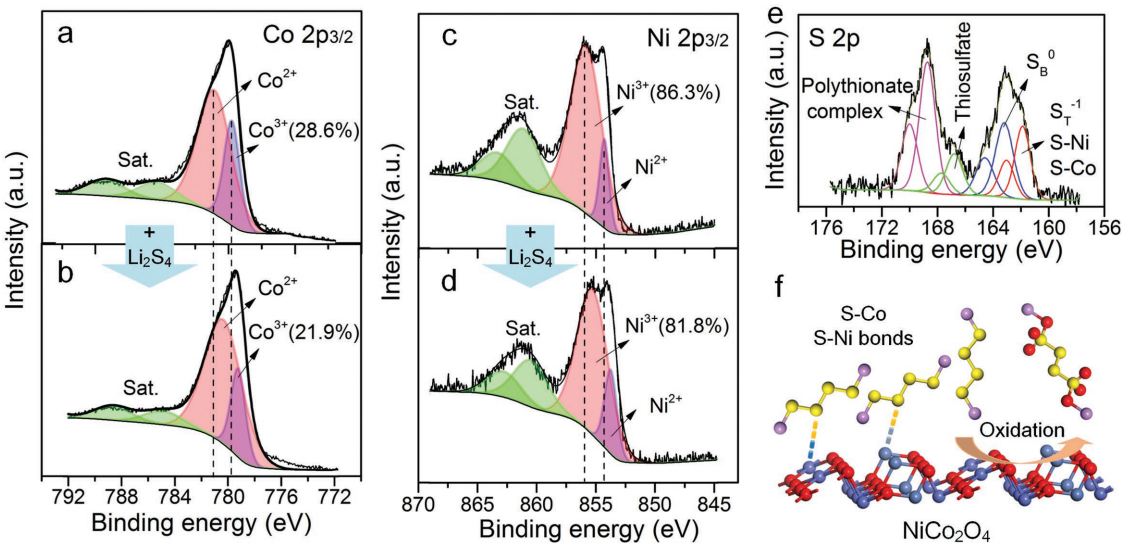

Figure 7. Chemical interactions between $NiCo_2O_4$ and LiPS. a–d) XPS spectra of the pristine $NiCo_2O_4$ and precipitate recovered from $Li_2S_4/NiCo_2O_4$ suspension. Co $2p_{3/2}$ core levels of (a) $NiCo_2O_4$ and (b) $Li_2S_4/NiCo_2O_4$, Ni $2p_{3/2}$ core levels of (c) $NiCo_2O_4$ and (d) $Li_2S_4/NiCo_2O_4$. e) S 2p core level of $Li_2S_4/NiCo_2O_4$. f) A schematic showing the chemical interaction between S and Ni/Co on the $NiCo_2O_4$ surface.

high tap density of 1.66 g cm^{-3}, close to the theoretical density (2.07 g cm^{-3}) of sulfur. Correspondingly, the $S/NiCo_2O_4$ composite delivers large volumetric capacity of 1867 mAh cm^{-3} at 0.1 C rate, almost twice that of the conventional S/carbon composite. Furthermore, polar TMOs offer good adsorption ability to LiPS to suppress the shuttle effect for the stable cycle performance. In particular, $NiCo_2O_4$ nanofibers could provide energetic reaction sites to catalyze conversion kinetics of soluble intermediate LiPS, followed subsequently by the strong adsorption of LiPS in the electrochemical dissolution–deposition processes. Therefore, this work provides a feasible strategy to fabricate carbon-free sulfur-based composite on the consideration of enhancing both the volumetric capacity and cycle performance of sulfur cathode. In comparison with conventional carbon materials, TMOs possess the unique advantages of high density, good adsorption, and favorable electrocatalytic activity, which are indispensable to insure the desirable performance of sulfur cathode. In the future, exploring for more efficient hosts based on design of density, electrical conductivity, electrocatalytic activity will lead to a great challenge for practical application of Li–S battery.

4. Experimental Section

Preparation of Hollow $NiCo_2O_4$ Nanofibers: The precursor solution was prepared by dissolving $Co(CH_3COO)_2{\cdot}4H_2O$ (1.8 mmol), $Ni(CH_3COO)_2{\cdot}4H_2O$ (0.9 mmol), and PAN (1 g) in N,N-dimethylformamide (DMF, 10 mL). Then, the pristine nanofibers were obtained by electrospinning the as-prepared solution at a flow rate of 2 mL h^{-1}. The distance and voltage between the nozzle and collector were 12 cm and 15 kV, respectively. The hollow $NiCo_2O_4$ nanofibers were obtained by calcining pristine nanofibers at 500 °C for 3 h in air. For comparison, CNFs were also prepared by electrospinning a DMF solution of PAN and polystyrene (PS) as reported previously.[7a]

Preparation of the $S/NiCo_2O_4$ Composite: Sulfur–amine chemistry was applied to precipitate sulfur on $NiCo_2O_4$ nanofibers. First, sublimed sulfur (400 mg) was dissolved in anhydrous ethanediamine (EDA, 16 mL) to form a black S-EDA solution. Then, $NiCo_2O_4$ nanofibers (120 mg) were dispersed in deionized water (200 mL), followed by adding into the S-EDA solution under vigorous stirring. Next, diluted HNO_3 was dropwise added into the above mixture until pH value reached to 7. Finally, the mixture was centrifuged, rinsed, and dried in vacuum to obtain the $S/NiCo_2O_4$ composite. The S/CNF composite was also prepared using the same method.

Materials Characterization: The morphology was characterized by scanning electron microscope (JEOL, JSM-7800F) and transmission electron microscope (JEOL, JEM-2800). The crystal structure was examined by X-ray diffraction (Rigaku mini FlexII). X-ray photoelectron spectroscopy (XPS) was performed on Thermo Scientific ESCALAB 250Xi. The sulfur content was determined by a TG curve (METTLER TOLEDO, TG/DSC1). The specific surface area was measured using Brunauer–Emmett–Teller method on JW-BK112 system. The volumes the $S/NiCo_2O_4$ or S/CNF composites were measured in the graduated glass cylinder with forceful shake and compression until the volume change measured was less than 2%. The tap density was then calculated by the ratio of weight to volume, which was expressed in g cm^{-3}.

Electrochemical Measurements: Cathodes were prepared by coating N-methyl pyrrolidone slurry (70 wt% $S/NiCo_2O_4$ or S/CNF, 20 wt% aligned carbon nanotubes (A-CNT) and 10 wt% polyvinylidene fluoride (PVDF)) on Al foil. CR2032 coin cells were assembled using the coated cathode, lithium metal anode, and Celgard 2300 separator. The electrolyte was composed of 1 M lithium bis(trifluoromethanesulfonyl)imide (LiTFSI) and 0.2 M $LiNO_3$ in 1,3-dioxolane (DOL) and 1,2-dimethoxyethane (DME) (1:1, v/v). The cell performance was further evaluated with different electrolyte/sulfur ratios (25, 20, 15, 10, and 5 µL mg^{-1}). The galvanostatic charge/discharge tests were performed in a potential cut-off window of 1.7–2.8 V (vs Li/Li^+) using LAND-CT2001A instruments. CV tests were carried out on an electrochemical station (CHI 600e). EIS were tested using an electrochemical station (Zahner IM6ex) in the frequency range of 10 mHz to 100 kHz, and the perturbation amplitude was 5 mV. All the capacity values were calculated on the mass of the $S/NiCo_2O_4$ composite or S/CNF composite. For symmetric cells, the electrode was prepared by casting a slurry of $NiCo_2O_4$/A-CNT or CNF/A-CNT (85 wt%) and PVDF (15 wt%) on Al foil. The weight ratio of $NiCo_2O_4$ or CNF to A-CNT (conducting agent) was identical to that in the sulfur cathode. The active materials loading was 1 mg cm^{-2} and 50 µL electrolyte was added. The electrolyte was composed of 1 M LiTFSI and 0.2 M Li_2S_6 in DOL and DME (1:1, v/v).

Adsorption Test of LiPS: Li_2S_4 solution (2 mmol L^{-1}) was prepared by adding Li_2S and S at a molar ratio of 1:3 in DME under vigorous stirring at 60 °C for 24 h. $NiCo_2O_4$ or CNF (50 mg) was added into Li_2S_4 solution (5 mL), and the supernatant was taken for photos and UV–vis absorption test ((UV–vis, Varian Cary 100 Conc) after 48 h. The precipitate was taken for XPS analysis. For visual transparent cell test, the cell was assembled by using a glass vessel (10 mL), lithium anode, $S/NiCo_2O_4$, and S/CNF cathodes in electrolyte (4 mL). The discharge rate was 0.05 C, and photos were taken at various DOD.

Supporting Information

Supporting Information is available from the Wiley Online Library or from the author.

Acknowledgements

Financial supports from the National Key Research and Development Program (2016YFB0100200), NFSC (21573114, 51502145 and 21421001) of China are gratefully acknowledged.

Conflict of Interest

The authors declare no conflict of interest.

Keywords

cathodes, chemical interactions, cycle stability, Li–S batteries, spinel nickel cobaltite, volumetric capacity

Received: November 11, 2018
Revised: December 31, 2018
Published online:

[1] a) X. P. Gao, H. X. Yang, *Energy Environ. Sci.* **2010**, *3*, 174; b) X. L. Ji, L. F. Nazar, *J. Mater. Chem.* **2010**, *20*, 9821.
[2] M. Hagen, D. Hanselmann, K. Ahlbrecht, R. Maça, D. Gerber, J. Tübke, *Adv. Energy Mater.* **2015**, *5*, 1401986.
[3] J. Zhang, H. Huang, J. Bae, S.-H. Chung, W. Zhang, A. Manthiram, G. Yu, *Small Methods* **2018**, *2*, 1700279.
[4] Y. X. Yin, S. Xin, Y. G. Guo, L. J. Wan, *Angew. Chem., Int. Ed.* **2013**, *52*, 13186.
[5] a) X. L. Ji, K. T. Lee, L. F. Nazar, *Nat. Mater.* **2009**, *8*, 500; b) B. Zhang, X. Qin, G. R. Li, X. P. Gao, *Energy Environ. Sci.* **2010**, *3*, 1531.
[6] a) J. C. Guo, Y. H. Xu, C. S. Wang, *Nano Lett.* **2011**, *11*, 4288; b) Z. Yuan, H. J. Peng, J. Q. Huang, X. Y. Liu, D. W. Wang, X. B. Cheng, Q. Zhang, *Adv. Funct. Mater.* **2014**, *24*, 6105.
[7] a) Z. Li, J. T. Zhang, Y. M. Chen, J. Li, X. W. Lou, *Nat. Commun.* **2015**, *6*, 8850; b) S. H. Chung, A. Manthiram, *Joule* **2018**, *2*, 710.
[8] a) Z. Zhang, L. L. Kong, S. Liu, G. R. Li, X. P. Gao, *Adv. Energy Mater.* **2017**, *7*, 1602543; b) L. W. Ji, M. M. Rao, H. M. Zheng, L. Zhang, Y. C. Li, W. H. Duan, J. H. Guo, E. J. Cairns, Y. G. Zhang, *J. Am. Chem. Soc.* **2011**, *133*, 18522.
[9] N. Jayaprakash, J. Shen, S. S. Moganty, A. Corona, L. A. Archer, *Angew. Chem.* **2011**, *123*, 6026.
[10] a) J. X. Song, M. L. Gordin, T. Xu, S. R. Chen, Z. X. Yu, H. Sohn, J. Lu, Y. Ren, Y. H. Duan, D. H. Wang, *Angew. Chem., Int. Ed.* **2015**, *54*, 4325; b) X. G. Sun, X. Wang, R. T. Mayes, S. Dai, *ChemSusChem* **2012**, *5*, 2079.
[11] a) X. Liang, C. Hart, Q. Pang, A. Garsuch, T. Weiss, L. F. Nazar, *Nat. Commun.* **2015**, *6*, 5682; b) Z. Li, B. Y. Guan, J. T. Zhang, X. W. Lou, *Joule* **2017**, *1*, 576; c) Y. Q. Tao, Y. J. Wei, Y. Liu, J. T. Wang, W. M. Qiao, L. C. Ling, D. H. Long, *Energy Environ. Sci.* **2016**, *9*, 3230; d) D. J. Xiao, H. Zhang, C. Chen, Y. Liu, S. Yuan, C. Lu, *ChemElectroChem* **2017**, *4*, 2959; e) L. Y. Hu, C. L. Dai, H. Liu, Y. Li, B. L. Shen, Y. M. Chen, S. J. Bao, M. W. Xu, *Adv. Energy Mater.* **2018**, *8*, 1800709; f) L. Kong, X. Chen, B. Q. Li, H. J. Peng, J. Q. Huang, J. Xie, Q. Zhang, *Adv. Mater.* **2018**, *30*, 1705219; g) Q. Sun, B. J. Xi, J. Y. Li, H. Z. Mao, X. J. Ma, J. W. Liang, J. K. Feng, S. L. Xiong, *Adv. Energy Mater.* **2018**, *8*, 1800595.
[12] a) H. B. Lin, L. Q. Yang, X. Jiang, G. C. Li, T. R. Zhang, Q. F. Yao, G. W. Zheng, J. Y. Lee, *Energy Environ. Sci.* **2017**, *10*, 1476; b) Z. Yuan, H. J. Peng, T. Z. Hou, J. Q. Huang, C. M. Chen, D. W. Wang, X. B. Cheng, F. Wei, Q. Zhang, *Nano Lett.* **2016**, *16*, 519; c) T. Chen, Z. W. Zhang, B. R. Cheng, R. P. Chen, Y. Hu, L. B. Ma, G. Y. Zhu, J. Liu, Z. Jin, *J. Am. Chem. Soc.* **2017**, *139*, 12710; d) J. Park, B. C. Yu, J. S. Park, J. W. Choi, C. Kim, Y. E. Sung, J. B. Goodenough, *Adv. Energy Mater.* **2017**, *7*, 1602567.
[13] a) Z. M. Cui, C. X. Zu, W. D. Zhou, A. Manthiram, J. B. Goodenough, *Adv. Mater.* **2016**, *28*, 6926; b) Z. H. Sun, J. Q. Zhang, L. C. Yin, G. J. Hu, R. P. Fang, H. M. Cheng, F. Li, *Nat. Commun.* **2017**, *8*, 14627; c) D. R. Deng, F. Xue, Y. J. Jia, J. C. Ye, C. D. Bai, M. S. Zheng, Q. F. Dong, *ACS Nano* **2017**, *11*, 6031.
[14] a) T. H. Zhou, Y. Zhao, G. M. Zhou, W. Lv, P. J. Sun, F. Kang, B. H. Li, Q. H. Yang, *Nano Energy* **2017**, *39*, 291; b) H. J. Peng, G. Zhang, X. Chen, Z. W. Zhang, W. T. Xu, J. Q. Huang, Q. Zhang, *Angew. Chem., Int. Ed.* **2016**, *55*, 12990.
[15] a) Y. R. Zhong, L. C. Yin, P. He, W. Liu, Z. S. Wu, H. L. Wang, *J. Am. Chem. Soc.* **2018**, *140*, 1455; b) J. H. Cheng, D. Zhao, L. S. Fan, X. Wu, M. X. Wang, N. Q. Zhang, K. N. Sun, *J. Mater. Chem. A* **2017**, *5*, 14519.
[16] X. Liang, Y. Rangom, C. Y. Kwok, Q. Pang, L. F. Nazar, *Adv. Mater.* **2017**, *29*, 1603040.
[17] a) D. H. Liu, C. Zhang, G. M. Zhou, W. Lv, G. W. Ling, L. J. Zhi, Q. H. Yang, *Adv. Sci.* **2018**, *5*, 1700270; b) J. Liang, L. C. Yin, X. N. Tang, H. C. Yang, W. S. Yan, L. Song, H. M. Cheng, F. Li, *ACS Appl. Mater. Interfaces* **2016**, *8*, 25193; c) Z. W. Zhang, H. J. Peng, M. Zhao, J. Q. Huang, *Adv. Funct. Mater.* **2018**, *28*, 1707536.
[18] a) H. Al Salem, G. Babu, C. V. Rao, L. M. R. Arava, *J. Am. Chem. Soc.* **2015**, *137*, 11542; b) Y. J. Li, J. M. Fan, M. S. Zheng, Q. F. Dong, *Energy Environ. Sci.* **2016**, *9*, 1998.
[19] Database of materials information by chemistry, composition, or property, https://www.materialsproject.org/ (accessed: January 2019).
[20] D. Ouyang, J. Y. Xiao, F. Ye, Z. F. Huang, H. Zhang, L. Zhu, J. Q. Cheng, W. C. H. Choy, *Adv. Energy Mater.* **2018**, *8*, 1702722.
[21] L. Fang, Z. Q. Jiang, H. T. Xu, L. Liu, Y. X. guan, X. Gu, Y. Wang, *J. Catal.* **2018**, *357*, 238.
[22] A. Iqbal, Z. Ali Ghazi, A. Muqsit Khattak, A. Ahmad, *J. Solid State Chem.* **2017**, *256*, 189.
[23] a) Q. Fan, W. Liu, Z. Weng, Y. M. Sun, H. L. Wang, *J. Am. Chem. Soc.* **2015**, *137*, 12946; b) H. W. Chen, C. H. Wang, W. L. Dong, W. Lu, Z. L. Du, L. W. Chen, *Nano Lett.* **2015**, *15*, 798.
[24] L. L. Li, S. J. Peng, Y. L. Cheah, P. F. Teh, J. Wang, G. Wee, Y. Ko, C. Wong, M. Srinivasan, *Chem. - Eur. J.* **2013**, *19*, 5892.
[25] L. Alexander, H. P. Klug, *J. Appl. Phys.* **1950**, *21*, 137.
[26] Z. Zhang, D. H. Wu, Z. Zhou, G. R. Li, S. Liu, X. P. Gao, *Sci. China Mater.* **2019**, *62*, 74.
[27] a) S. H. Chung, A. Manthiram, *Adv. Mater.* **2018**, *30*, 1705951; b) Q. Pang, X. Liang, C. Y. Kwok, J. Kulisch, L. F. Nazar, *Adv. Energy Mater.* **2017**, *7*, 1601630.
[28] a) G. M. Zhou, H. Z. Tian, Y. Jin, X. Y. Tao, B. F. Liu, R. F. Zhang, Z. W. Seh, D. Zhuo, Y. Y. Liu, J. Sun, J. Zhao, C. X. Zu, D. S. Wu, Q. F. Zhang, Y. Cui, *Proc. Natl. Acad. Sci. U. S. A.* **2017**, *114*, 840;

b) X. Y. Tao, J. G. Wang, C. Liu, H. T. Wang, H. B. Yao, G. Y. Zheng, Z. W. Seh, Q. X. Cai, W. Y. Li, G. M. Zhou, C. X. Zu, Y. Cui, *Nat. Commun.* **2016**, *7*, 11203.

[29] a) L. M. Tao, Y. B. Li, M. Li, G. Y. Gao, X. Xiao, M. K. Wang, X. X. Jiang, X. W. Lv, Q. W. Li, S. S. Zhang, Z. X. Zhao, C. Zhao, Y. Shen, *J. Phys. Chem. C* **2017**, *121*, 25888; b) Y. S. Fu, C. Q. Peng, D. S. Zha, J. W. Zhu, L. L. Zhang, X. Wang, *Electrochim. Acta* **2018**, *271*, 137.

[30] a) C. Barchasz, F. Molton, C. Duboc, J.-C. Leprêtre, S. Patoux, F. Alloin, *Anal. Chem.* **2012**, *84*, 3973; b) Y. J. Li, H. Zhan, S. Q. Liu, K. L. Huang, Y. H. Zhou, *J. Power Sources* **2010**, *195*, 2945.

[31] K. T. Ng, D. M. Hercules, *J. Phys. Chem.* **1976**, *80*, 2094.

[32] a) K. M. Abraham, S. M. Chaudhri, *J. Electrochem. Soc.* **1986**, *133*, 1307; b) B. J. Lindberg, K. Hamrin, G. Johansson, U. Gelius, A. Fahlman, C. Nordling, K. Siegbahn, *Phys. Scr.* **1970**, *1*, 286.

[33] X. Liang, C. Y. Kwok, F. Lodi Marzano, Q. Pang, M. Cuisinier, H. Huang, C. J. Hart, D. Houtarde, K. Kaup, H. Sommer, T. Brezesinski, J. Janek, L. F. Nazar, *Adv. Energy Mater.* **2016**, *6*, 1501636.

[34] Y. R. Zhong, K. R. Yang, W. Liu, P. He, V. Batista, H. L. Wang, *J. Phys. Chem. C* **2017**, *121*, 14222.

[35] Y. Chen, S. Choi, D. W. Su, X. C. Gao, G. X. Wang, *Nano Energy* **2018**, *47*, 331.

[36] J. Xu, W. X. Zhang, Y. Chen, H. B. Fan, D. W. Su, G. X. Wang, *J. Mater. Chem. A* **2018**, *6*, 2797.

[37] J. Xu, W. X. Zhang, H. B. Fan, F. L. Cheng, D. W. Su, G. X. Wang, *Nano Energy* **2018**, *51*, 73.

[38] D. W. Su, M. Cortie, H. B. Fan, G. X. Wang, *Adv. Mater.* **2017**, *29*, 1700587.

[39] D. W. Su, M. Cortie, G. X. Wang, *Adv. Energy Mater.* **2017**, *7*, 1602014.

[40] J. Xu, T. Lawson, H. B. Fan, D. W. Su, G. X. Wang, *Adv. Energy Mater.* **2018**, *8*, 1702607.

[41] a) H. K. Jing, L. L. Kong, S. Liu, G. R. Li, X. P. Gao, *J. Mater. Chem. A* **2015**, *3*, 12213; b) D. D. Han, S. Liu, Y. T. Liu, Z. Zhang, G. R. Li, X. P. Gao, *J. Mater. Chem. A* **2018**, *6*, 18627.